Peer reviewed version

Link to published version (if available):
10.2514/6.2017-3364

Link to publication record in Explore Bristol Research
PDF-document

University of Bristol - Explore Bristol Research
General rights

Experimental Investigation of Flow Around Three-Element High-Lift Airfoil with Morphing Fillers

Hasan Kamliya Jawahar[*], Mahdi Azarpeyvand[†]
University of Bristol, Bristol, United Kingdom, BS8 1TR
and
Carlos R. Ilário da Silva[‡]
Embraer, São José dos Campos, 12227-901, Brazil

Aerodynamic and aeroacoustic measurements of a three-element airfoil (30P30N) fitted with various slat cove fillers and droop-slat configuration were carried out for a wide range of angles of attack and Reynolds numbers (4.6×10^5 to 1.1×10^6). The results are presented for static and unsteady surface pressure measurements and flow visualisation using particle image velocimetry. Mean surface pressure measurement results show that the aerodynamic performances were affected with the application of slat cove filler especially if its profile was not apt for the operating conditions. The PIV results clearly show that a highly energised fixed vorticity was present within the slat cove region of the baseline case and it was eliminated by the application of slat cove filler. A smaller vorticity develops as a result of the slat cove filler and the vortices size changes with increase in angle of attack. The wall-pressure spectra acquired using the flush mounted transducers shows narrowband and broadband components for the baseline case. The application of slat cove fillers completely eliminated the narrowband spectra generated by the vortices inside the slat cove. However, the slat cove filler appears to increase the overall broadband at low and mid-frequency range in the airfoil near-field. Results confirmed the great aerodynamic and aeroacoustic potential of the morphing structures for high-lift devices, which is one of the highly sought candidate for the next generation aircraft control surfaces.

Nomenclature

c	=	stowed chord length, m
C_l	=	lift coefficient
$C_{l,max}$	=	maximum lift coefficient
C_p	=	pressure coefficient
f	=	frequency, Hz
G	=	auto-spectral density function, Pa^2/Hz
l	=	span length, m
p_{ref}	=	reference pressure ($= 2 \times 10^5$), Pa
Re_c	=	chord based Reynolds number
RMS	=	root mean squared
TKE	=	turbulence kinetic energy
U_∞	=	free stream velocity, m/s
$\overline{u'u'}$	=	streamwise Reynolds normal stress component
$\overline{v'v'}$	=	crosswise Reynolds normal stress component
x, y, z	=	streamwise, crosswise, spanwise Cartesian coordinates, mm
α	=	angle of attack, °
$\gamma^2_{p_i p_j}$	=	coherence function
Φ_{pp}	=	wall-pressure power spectral density, Pa^2/Hz

[*]PhD Student, Department of Aerospace Engineering, AIAA Student Member, `hasan.kj@bristol.ac.uk`
[†]Senior Lecturer and Royal Academy of Engineering Research Fellow, Department of Mechanical Engineering, `m.azarpeyvand@bristol.ac.uk`
[‡]Technology Development Engineer, Embraer, Sáo José dos Campos, Brazil, `carlos.ilario@embraer.com.br`

I. Introduction

THE impact on aircraft noise on the communities near the airport has been an issue since the entry of turbofan and turbojet engines into civil aviation from the 1960s and 1970s. The widespread global expansion of air travel has made the environmental impact of aircraft noise much more prominent in the recent times. This has forced the International Civil Aviation Organisation (ICAO) to set technical standards for civil air transport aircraft and 180 countries have adapted this. With such upcoming regulations to reduce noise impact on communities near airport further understanding into aircraft noise has to be achieved. The introduction of high bypass-ratio turbofans engines into civil aircrafts have drastically reduced engine noise over the last several decades, making the airframe noise the same magnitude as that of the engine noise especially during the landing phase. One of the prominent sources of airframe noises are the high-lift devices namely the slats and flaps. In order to reduce these prominent noise sources several passive and active flow control methods have been investigated in the past it includes morphing structures [1,2], porous materials [3,4], surface treatments [5] and serrations [6–8].

Previous tests by other researchers have shown that the broadband and tonal noise from conventional slat and wing configurations are created from the unsteady flow within the slat cove region originating from the slat cusp and vortex shedding from the slat trailing edge. Several experimental and computational studies [9–18] were made over the past decade to reduce the broadband noise arising from the slat cove region by filling the recirculation area within the slat cove gap. Even though reduction in broadband noise was observed at all the instances it has been a challenge to maintain the aerodynamic performance of the high-lift device for the cove filled configurations.

The approach of filling the slat cove gap to reduce noise is based on eliminating the strong shear layer created after the cusp and avoiding the development of complicated flow structure within the cove region by using a smoothly contoured profile. Horne *et al.* from NASA in order to eliminate the unsteady recirculation region within the slat cove tested a solid slat cove filler (SCF) on a Boeing 777-200 semi span model in the NASA Ames 40 by 80 foot Wind Tunnel. The slat cove filler profiles were derived from CFD analysis in order to maintain attached flow on the slat lower surface. From the experiments it was shown that slat cove filler was effective in reducing broadband slat noise upto 4-5 dB [9] that was measured using a microphone phased array. However no aerodynamic measurements were presented in this study. Streertt *et al.* further investigated noise and basic aerodynamics of the SCF setup using trapezoidal wing swept model fitted [10]. The results showed noise reduction to be sensitive to the angle of attack and SCF modification. The SCF modification showed a reduction of 3-5 dB over a wide spectrum. The aerodynamic performance appeared slightly better than the baseline at angles of attack below 20° and stall occurred 2 degrees earlier compared to baseline. The specific reason of the aerodynamic performance loss was not pointed out due to the lack of aerodynamic data such as detailed surface pressure and wake shear layer measurements.

Imamura *et al.* and Ura *et al.* from JAXA showed experimentally and computationally [13, 14] that even though noise reduction can be achieved by the use of SCF, its profile significantly affects the aerodynamic lift characteristics of the three-element airfoil. They tested two SCF profiles that were designed based on the flow field streamlines of angles of attack 0° and 8° on a MDA 30P30N airfoil. Eventhough the results showed a reduction of 5 dB for both the cases they found that the aerodynamic lift characteristics performance were same as that of the baseline for only the SCF profile made from flow field streamlines of angle of attack 8° whereas the SCF profile made from angle of attack 0° stalls prematurely. Tao and Sun [18] in a very recent optimisation study performed several DES simulations using 44 configurations of SCF profile designs aimed to produce maximum lift coefficient for fixed design point with angle of attack of 22° and $Re_c = 9 \times 10^6$. The final optimised SCF profile showed a reduction in noise while maintaining aerodynamic performance.

Eventhough several studies [9–18] have been performed on the noise reduction capabilities of the slat cove filler, only basic aerodynamic and noise measurements have been presented. A detailed experimental study of the aerodynamic performance characteristics such as surface pressure measurements, shear layer measurements and the interaction confluent wakes of all the three-element of the high-lift airfoil has not yet been reported. As part of the current study PIV measurements and unsteady surface pressure of the aforementioned aerodynamic behaviour of the slat cove filler will be studied in detail in order to try and improve the aerodynamic behaviour and reduce noise generation of the traditional three-element airfoil.

II.   Experimental Setup

A.   Experimental and Wind-Tunnel Setup

The aerodynamic and aeroacoustic measurements of the 30P30N three-element airfoil was carried out in the low-turbulence wind-tunnel facility at the University of Bristol. The low-turbulence wind-tunnel facility has an octagonal working section of 0.8 m × 0.6 m × 1 m and has a contraction ratio of 12:1. The wind-tunnel is capable of maximum velocity of up to 100 m/s and with turbulence level as low as 0.05%. This wind-tunnel is also equipped with Particle Image Velocimetry (PIV). The working section is constructed with interchangeable transparent glass windows allowing wide possibilities for the placement of the laser and the camera.

1.   Static Pressure Measurements Setup

MicroDaq pressure scanners manufactured by Chell Instruments were used for static surface pressure measurements. Two scanners equipped with 32 channels were used to measure the surface pressure. The scanners have a full scale measuring capacity of 1 Psi with system accuracy of ±0.05%. The measurements were made with a frequency of 500 Hz and the data was collected for 60 s.

2.   Unsteady Pressure Measurements Setup

FG-3329-P07 from Knowles Electronics were used for unsteady surface pressure measurements. This transducer was selected for measurement as it has been proven successful in previous experiments carried out by Garcia [19–21] on NACA 0012 airfoil. The transducer has a diameter of 2.5 mm and a height of 2.5 mm with a sensing area of 0.8 mm. The FG-3329-P07 transducer has a manufacture provided sensitivity of 22.4 mV/Pa (45 Pa/V) in the flat region of the transducer response. From the calibration of the transducer installed in the wing the transducer sensitivity varied between 20.2 mV/Pa and 23.5 mV/Pa. The unsteady surface pressure measurements using FG transducers were carried out for $t = 32$ s using a sampling frequency of $f = 40$ kHz.

3.   Particle Image Velocimentry Setup

The flow structure within and around the slat and flap cove region of the three-element airfoil were studied using two-dimensional two-component Particle Image Velocimetry (PIV) in the low turbulence closed-circuit wind tunnel. A Dantec DualPower 200 mJ Nd:YAG laser with a wavelength of 532 nm was used to produce 1 mm thick laser sheet with the time interval between each snapshots of 9 μs and a repetition rate of 10 Hz. A mixture of Polyethylene glycol 80 with a mean diameter of 1 μm were used to seed the air inside the low turbulence wind tunnel. A total number of 2400 images for each measurement were captured using a FlowSense 4 MP CCD camera with a resolution of 2078 × 2078 pixels and 14 bit, corresponding to field view of 6.3 cm × 6.3 cm. The images were analysed with the DynamicStudio software from Dantec. The iterative process yield grid correlation window of 16 × 16 pixels with an overlap of 50%, resulting in a facial vector spacing of 0.23 mm.
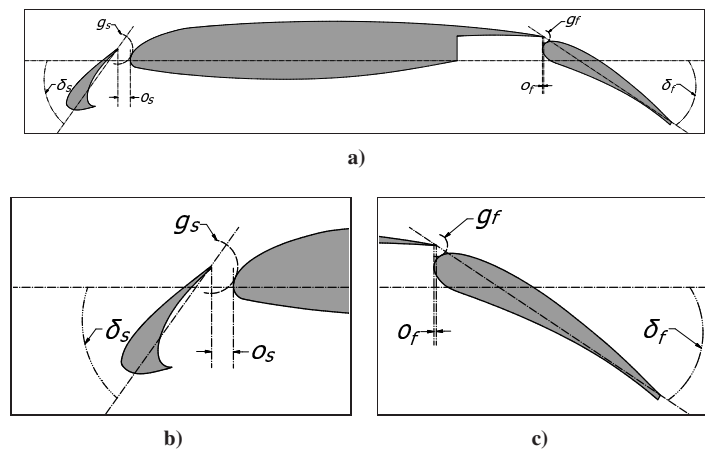

Figure 1. MDA 30P30N three-element high-lift airfoil geometric parameters.

American Institute of Aeronautics and Astronautics

B. 30P30N Three-Element High-Lift Airfoil Setup

An MDA 30P30N three-element high-lift airfoil with a retracted chord of $c = 0.35$ m and a span of $l = 0.53$ m was manufactured using a computer aided numerically controlled machine. In order to maintain two-dimensionality within the slat cove and flap cove regions, no brackets were used on the spanwise direction. All the three-elements were held together by steel clamps on the sides of the airfoil. FG-3329-P07 transducers have been installed in all the three element of the wing for the measurement unsteady surface pressure on the MDA airfoil (see Fig. 4 & Table. 2). The MDA airfoil has also been equipped with a large number of static pressure taps (103) placed along the mid-span of the airfoil, which can also be used for remote sensing using pressure transducers.

1. Slat Cove Filler Design

As part of the noise reduction study of the MDA airfoil, a slat cove filler (SCF) has been designed using similar strategy introduced by Imamura *et al.* [13, 14] for experimentation purposes. Initially, preliminary RANS steady state simulations for the Baseline case were performed at the angle of attack 8°, the turbulent kinetic energy (TKE) contours (see Fig. 3) were then plotted and the profile with high TKE indicating the slat shear layer trajectory was carefully and manually extracted and was used for defining the shape of the SCF profile. Another configuration with a Half SCF (H-SCF) has also been considered, which exhibits good aerodynamic and noise reduction properties as shown computationally by Tao [18]. Both the slat cove fillers were manufactured using 3D printing machines and was manufactured in four different sections that could be slided along the span of the slat. The SCF is fitted with 6 pressure taps along the mid-span of the wing for surface pressure measurements.
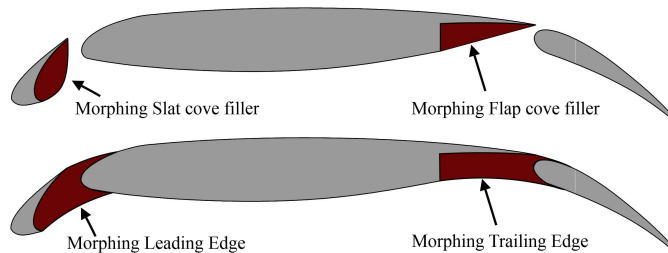

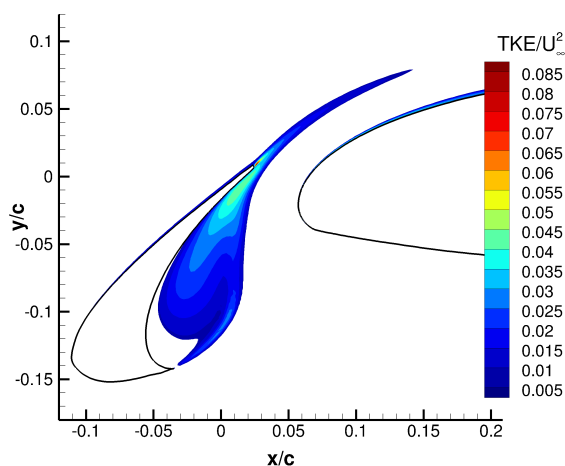**Figure 2. Morphing cove fillers for slat and flap (top) and morphing leading edge and trailing edge.**

Figure 3. Turbulent kinetic energy contours indicating slat shear layer profiles around 30P30N airfoil slat for an angle of attack, $\alpha = 8°$ at $Re_c = 1.7 \times 10^6$

American Institute of Aeronautics and Astronautics

Table 1. Geometrical parameters in percentage of stowed airfoil chord, $c = 0.35$ m.

Slat chord	c_s	$0.15c$
Main-element chord	c_{me}	$0.83c$
Flap chord	c_f	$0.3c$
Slat deflection angle	δ_s	30°
Flap deflection angle	δ_f	30°
Slat gap	g_s	2.95%
Flap gap	g_f	1.27%
Slat overhang	o_s	−2.5%
Flap overhang	o_f	0.25%

Table 2. Pressure transducer locations on the MDA 30P-30N airfoil.

	No.	x (mm)	z (mm)
Main-Element	M1	22.414	277
	M2	22.414	280.6
	M3	22.414	288.4
	M4	22.414	301.4
	M5	22.414	319.6
	M6	239.701	277
Flap	F1	308.844	277
	F2	308.844	280.6
	F3	308.844	288.4
	F4	308.844	301.4
	F5	308.844	319.6
	F6	349.301	277
	F7	349.301	280.6
	F8	349.301	288.4
	F9	349.301	301.4
	F10	349.301	319.6
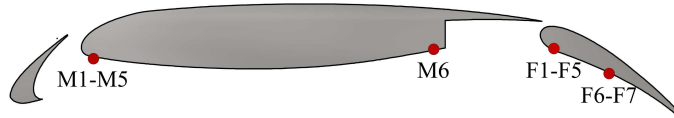
Figure 4. Surface transducer locations on the MDA 30P-30N airfoil.
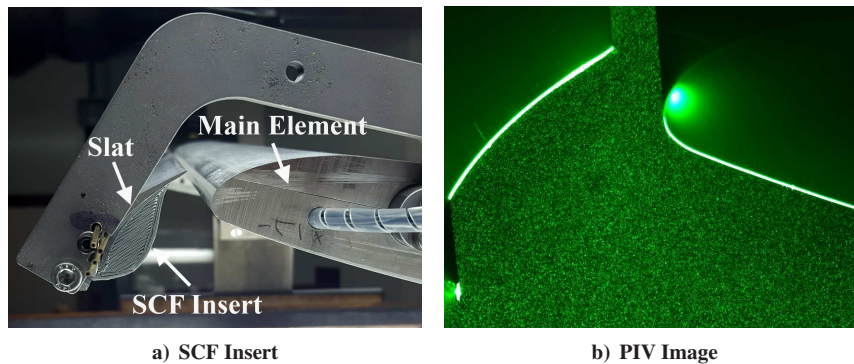

a) SCF Insert

b) PIV Image

Figure 5. 3D printed slat cove filler (SCF) section installed on the slat and reduced surface reflection during PIV by the use of black self adhesive vinyl sheet.

III. Results and Discussion

A. Aerodynamic Measurements

Experimental studies using an MDA 30P30N three-element airfoil with a retracted chord of $c = 0.35$ m and span of $l = 0.53$ m were carried out in the low turbulence closed circuit wind-tunnel facility at the University of Bristol. The airfoil was tested for a wide range of angles of attack from, $\alpha = 0°$ to $15°$ for wide range of flow velocities 20, 30, 40 and 47 m/s. The tested configurations were the Baseline, Slat cove filler (SCF) and Droop-slat cases, as shown in Fig. 2. The MDA airfoil was equipped with 103 pressure taps to accurately capture the surface pressure distribution. For the purpose of brevity only four angles of attack, $\alpha = 6°, 8°, 10°$ and $12°$, with a flow velocity of $U_\infty = 30$ m/s, corresponding to a chord based Reynolds number of $Re_c = 7 \times 10^5$, are presented here.

1. Pressure coefficient distribution

The pressure coefficient C_p distribution calculated from the mean surface pressure measurements acquired along the mid-span of the Baseline case, for the tested chord based Reynolds numbers $Re_c = 4.9 \times 10^5, 7.0 \times 10^5, 9.3 \times 10^5$ and 1.1×10^6 are presented in Fig. 6. The results show that the changes in C_p distribution over the slat and main-element are insignificant at the tested Reynolds numbers. An increase only in the order of 5% on the suction peak (C_p) of the main-element was observed for $Re_c = 1.2 \times 10^6$ relative to $Re_c = 4.9 \times 10^5$, whereas the changes on the suction peak of the flap were up to 10% higher for $Re_c = 1.1 \times 10^6$. Valarezo [22, 23] showed that the effects of Reynolds number on the lift of multi-element airfoil was very evident for flow conditions below $Re_c = 4 \times 10^6$. They also showed a considerable increase in the maximum lift between $Re_c = 2 \times 10^6$ and 9×10^6 at a Mach number of 0.2. The effects of Reynolds number and its significance on lift of high-lift airfoil was also showed by Chin *et al* [24] and they also discussed the increased effect of Reynolds number on the suction peak of the flap.
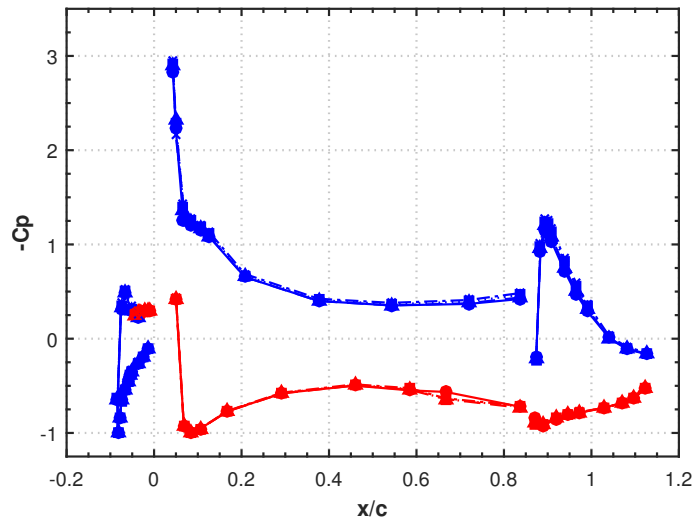

Figure 6. Coefficient of pressure distribution over 30P30N Baseline airfoil at angle of attack $\alpha = 8°$.

Suction side — and Pressure side — for flow velocity of $U_\infty = 20$ m/s ($Re_c = 4.6 \times 10^5$): Circles with solid lines; $U_\infty = 30$ m/s ($Re_c = 7.0 \times 10^5$): Triangles with dashed lines; $U_\infty = 40$ m/s ($Re_c = 9.3 \times 10^5$): Squares with dotted lines; $U_\infty = 47$ m/s ($Re_c = 1.1 \times 10^6$): Crosses with dotted-dashed lines.

The pressure distribution with respect to model the coordinates for the Baseline case at the tested angles of attack $\alpha = 6°, 8°, 10°$ and $12°$ are presented in Fig. 7. The change in C_p distribution is very evident especially on the suction side of the main-element as the angle of attack is increased. The loading on the slat and main-element increases with the angle of attack. The increased suction peak on the main-element at higher angles of attack is due to the higher velocity from the increased mass flow through the slat gap as the angle of attack is increased. The suction peak on the upper surface increases up to 30% on the main-element and 20% on the flap for $\alpha = 12°$ relative to $\alpha = 6°$.

Figures 9 and 10 show the pressure coefficient C_p for the Baseline, SCF and Droop-slat configurations. The results in Fig. 9 show that the modifications on the slat such as SCF affect the suction peak on the main-element of the airfoil. The Baseline case has the highest suction peak for both the presented angles of attack. The suction peak on the main-element for the SCF was reduced by $\approx 16\%$ at $\alpha = 6°$ and $8°$ and by $\approx 26\%$ at $\alpha = 10°$ and $12°$. The results for the slat in Fig. 10 shows that the C_p on the pressure side remains unchanged for the Baseline case but for the SCF changes
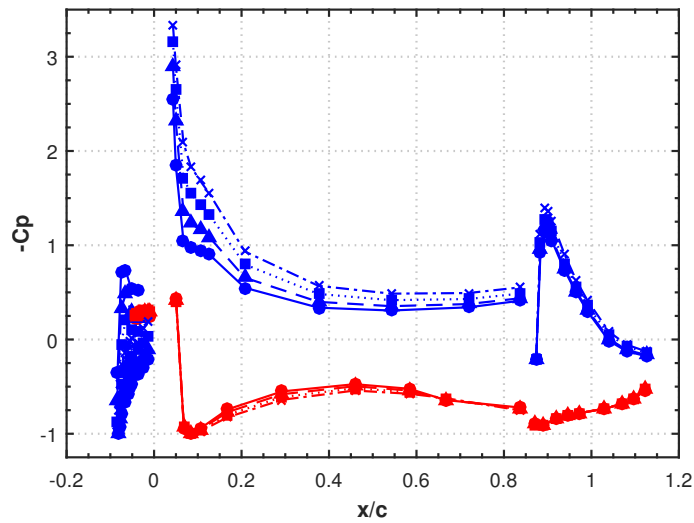
Figure 7. Coefficient of pressure distribution over 30P30N Baseline airfoil for a flow velocity of $U_\infty = 30$ m/s, $Re_c = 7.0 \times 10^5$.

Suction side — and Pressure side — for $\alpha = 6°$: Circles with solid lines; $\alpha = 8°$: Triangles with dashed lines; $\alpha = 10°$: Squares with dotted lines; $\alpha = 12°$: Crosses with dotted-dashed lines.

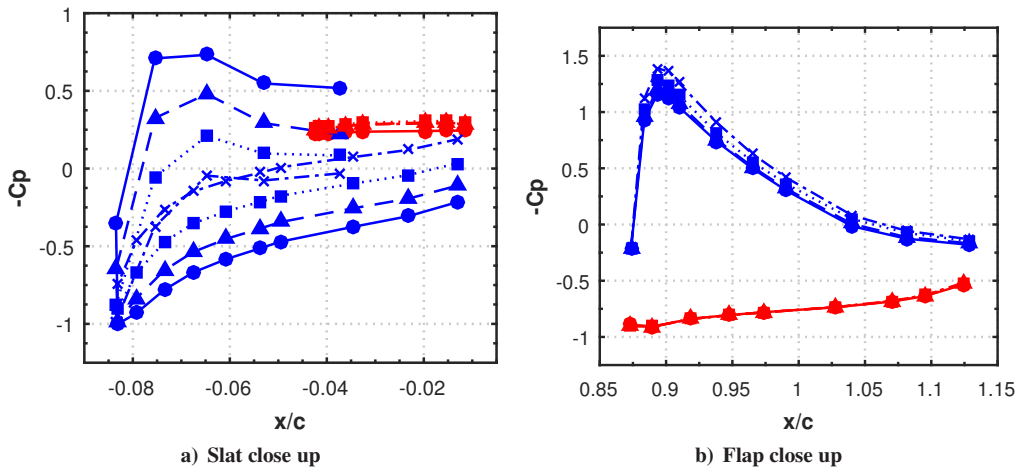a) **Slat close up**

b) **Flap close up**

Figure 8. Coefficient of pressure distribution over 30P30N Baseline airfoil around the slat and flap region for a flow velocity of $U_\infty = 30$ m/s, $Re_c = 7.0 \times 10^5$.

Suction side — and Pressure side — for $\alpha = 6°$: Circles with solid lines; $\alpha = 8°$: Triangles with dashed lines; $\alpha = 10°$: Squares with dotted lines; $\alpha = 12°$: Crosses with dotted-dashed lines.

quite significantly as the angle of attack is increased. The suction peak near the slat cusp is increased for the SCF relative to the Baseline by up to 30% for the presented angles of attack. This is due to the absence of sudden pressure gradient and the increased velocity due to the streamline profile of the SCF. The absence of slat gap in the Droop-slat configuration results in a completely different C_p distribution relative to the other two cases, as seen in Figs. 9 and 10. At $\alpha = 6°$ and $8°$ the Droop-slat configuration does not create any lift on the very leading edge ($x/c \approx -0.08$ to 0) due to the high angle of deflection ($\delta_{Droop} = 30°$) of the leading edge. However, as the angle of attack increases the Droop-slat configuration produces more lift. The suction peak over the Droop-slat at the same chord locations as that of the Baseline and the SCF cases are drastically reduced ($\approx 54\%$) due to the absence of the re-energized flow from the slat gap. The C_p measurements over the flap for the presented angles of attack remains unchanged for the Baseline and SCF cases. However, for the Droop-slat configuration it increases up to 7.5%. The changes to the slat for the tested range of Reynolds number and angles of attack does not affect the separation on the flap. Previous studies on MDA airfoil has shown that the confluent boundary layers arising from the slat and main-element plays a major role on the delayed separation over the flap.
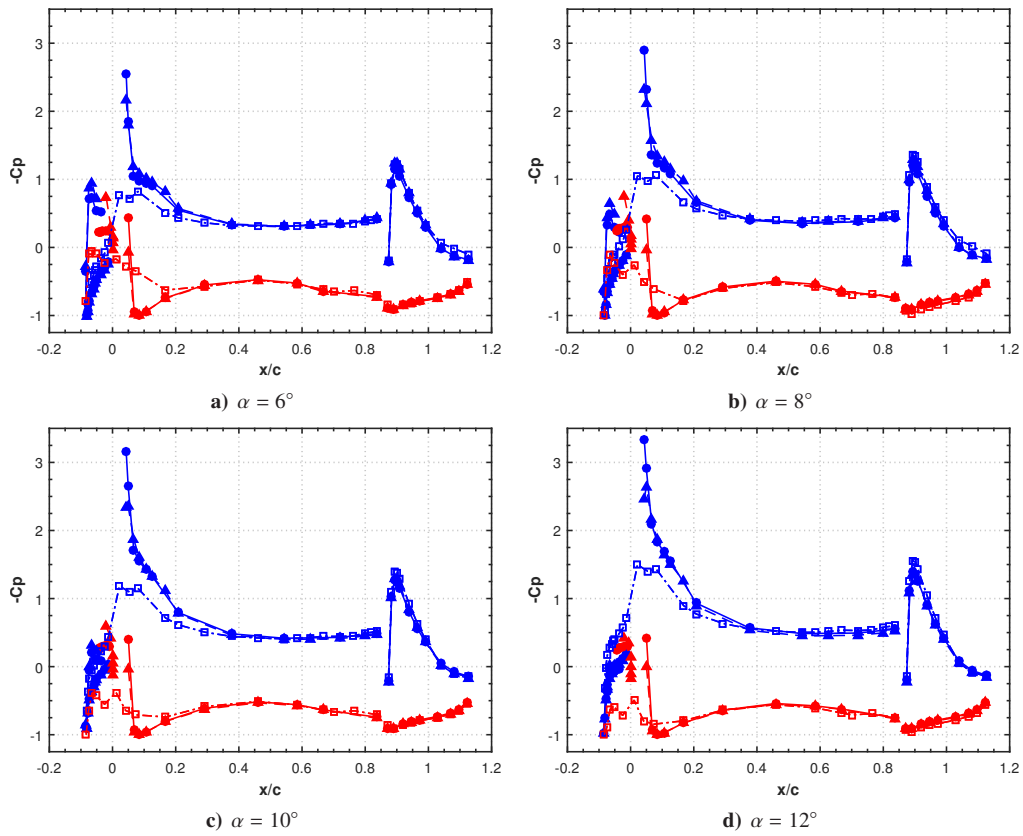
American Institute of Aeronautics and Astronautics

Figure 9. Coefficient of pressure distribution over 30P30N airfoil with slat modifications, for a flow velocity of $U_\infty = 30$ **m/s,** $Re_c = 7.0 \times 10^5$**.**

Suction side —— and Pressure side —— for Baseline: Circles with solid lines; Slat Cove Filler: Triangles with dashed lines; Droop-slat: Squares with dotted-dashed lines.
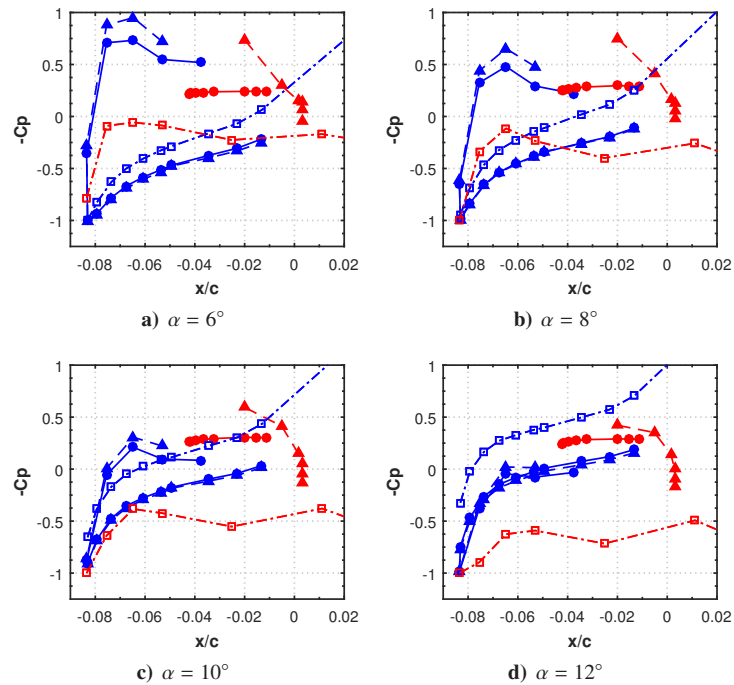

Figure 10. Coefficient of pressure distribution over 30P30N airfoil with slat modifications, for a flow velocity of $U_\infty = 30$ **m/s,** $Re_c = 7.0 \times 10^5$**.**

Suction side —— and Pressure side —— for Baseline: Circles with solid lines; Slat Cove Filler: Triangles with dashed lines; Droop-slat: Squares with dotted-dashed lines.

American Institute of Aeronautics and Astronautics
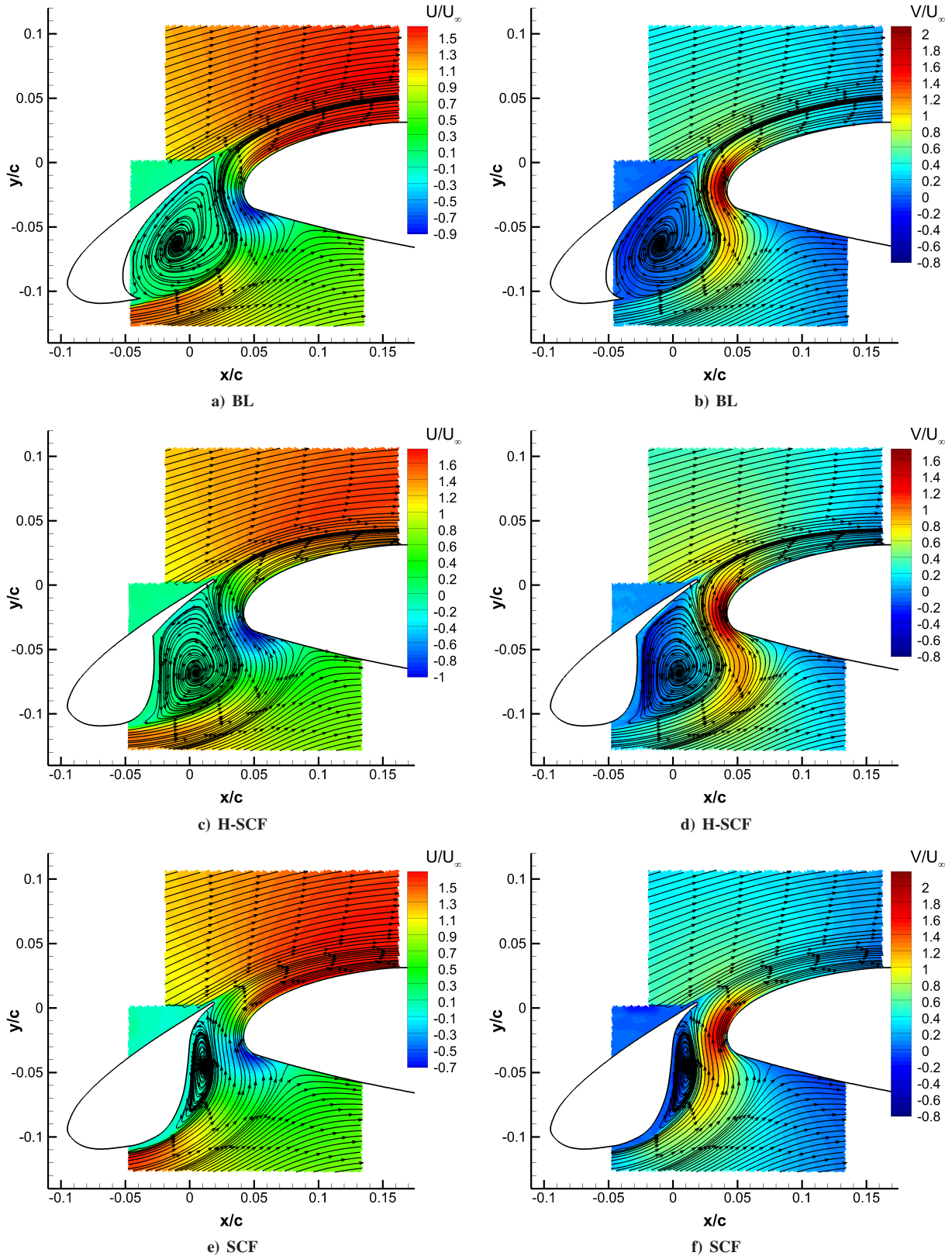
B.   Flow Visualisation

Figure 11. PIV flow visualisation of the mean streamwise and crosswise velocity components around the slat region for $\alpha = 6°$ **with a flow velocity of** $U_\infty = 30$ **m/s,** $Re_c = 7.0 \times 10^5$**.**
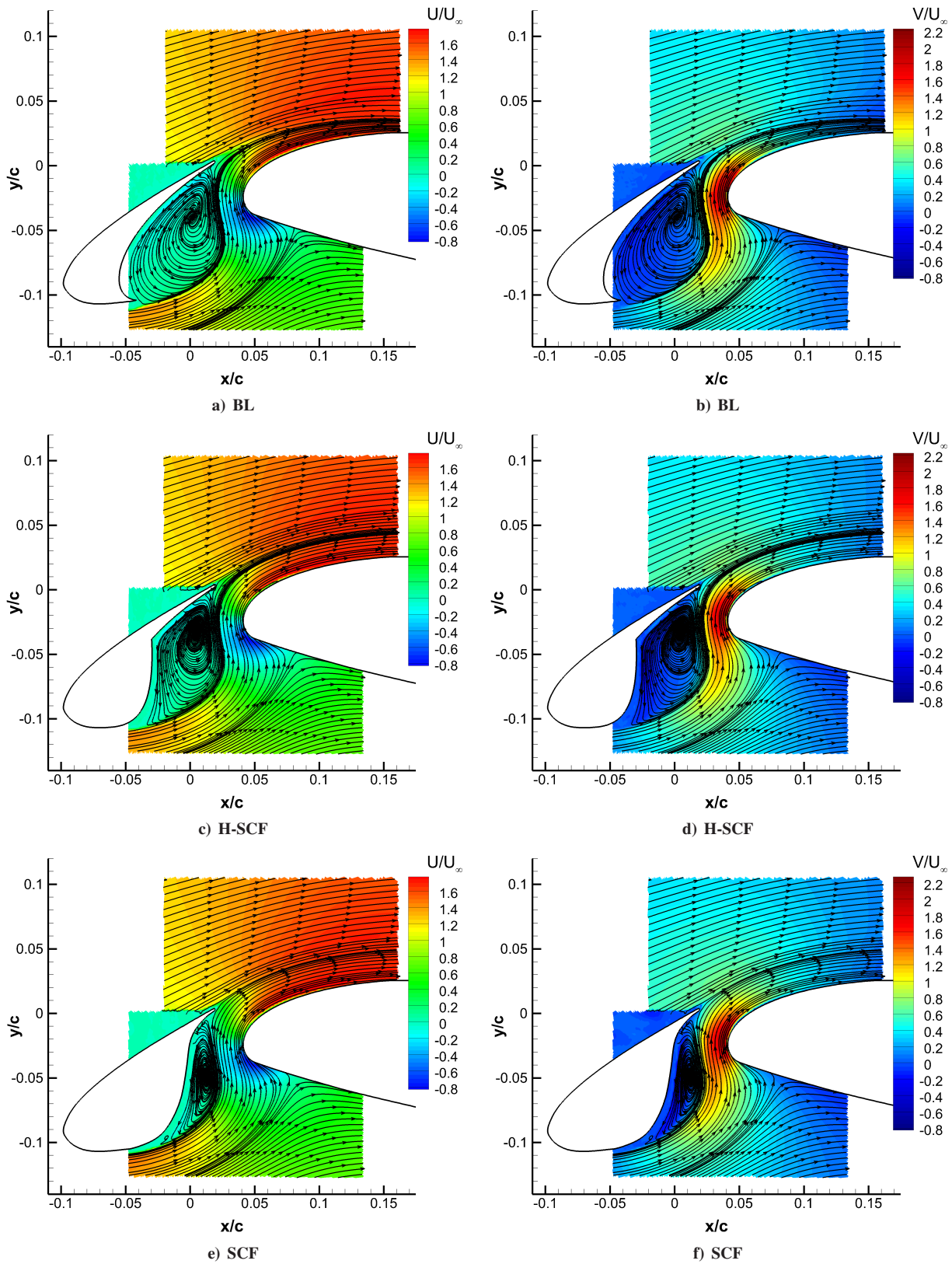
Figure 12. PIV flow visualisation of the mean streamwise and crosswise velocity components around the slat region for $\alpha = 8°$ with a flow velocity of $U_\infty = 30$ m/s, $Re_c = 7.0 \times 10^5$.

Figure 13. PIV flow visualisation of the mean streamwise and crosswise velocity components around the slat region for $\alpha = 10°$ with a flow velocity of $U_\infty = 30$ m/s, $Re_c = 7.0 \times 10^5$.
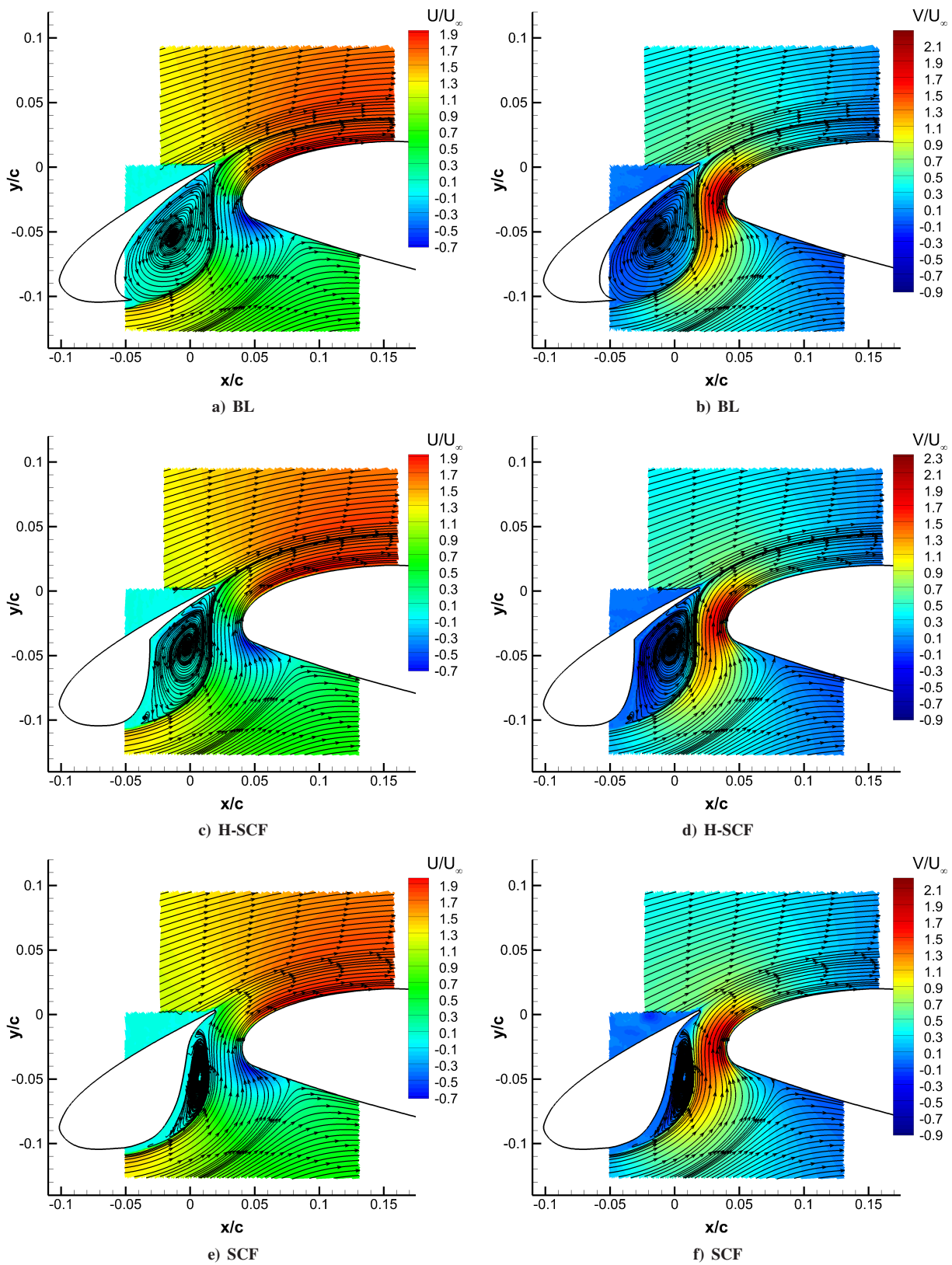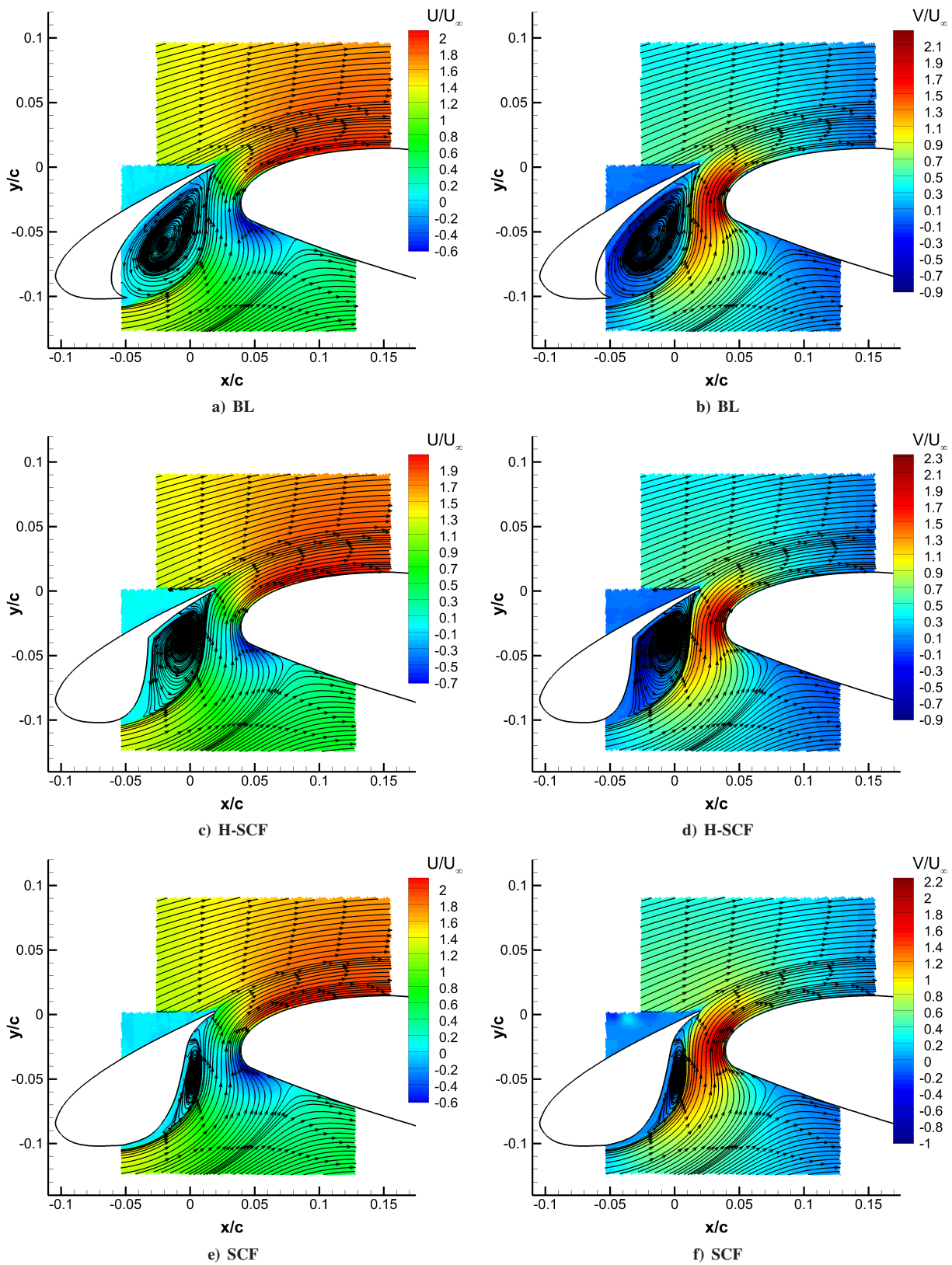
Figure 14. PIV flow visualisation of the mean streamwise and crosswise velocity components around the slat region for $\alpha = 12°$ **with a flow velocity of** $U_\infty = 30$ **m/s,** $Re_c = 7.0 \times 10^5$**.**

American Institute of Aeronautics and Astronautics

Detailed particle image velocimetry (PIV) studies were performed in and around the slat region for the Baseline, H-SCF and SCF cases at the angles of attack $\alpha = 6°$, $8°$, $10°$ and $12°$ with a flow velocity of $U_\infty = 30$ m/s ($Re_c = 7.0 \times 10^5$). Figures 11 to 14 show the contours of the mean streamwise and crosswise velocity distribution close to the slat region with streamlines showing the flow direction for all the Baseline, H-SCF and SCF cases. For the Baseline case it can be seen that the shape and structure of the fixed vortices present within the slat cove region were largely influenced by the angle of attack. The magnitude of the negative velocity that arises right after the flow impingement on the main-element appears to be greatly influencing the trajectory of the slat shear layer leaving the slap cusp. At $\alpha = 6°$, the vortices appears to be the largest as the slat shear layer impinges at the very end of the slat trailing-edge and majority of the flow moves towards the trailing-edge and mixes into the free stream. The impingement point of the slat shear layer on the slat lower surface moves away from the slat trailing-edge towards the slat mid-chord as the angle of attack is increased. This slat shear layer trajectory with a much shorter path before the impingement restricts the recirculation area at increased angles of attack. This decreased recirculation area and increased crosswise velocity results in the higher vorticity velocity inside the slat cove region. The increased mass flow through the slat gap along with the higher negative velocity on the main-element appears to be the key factors influencing this movement of the slat shear layer trajectory with angle of attack. The contours show negative velocity inside the slat cove region, which can be associated with the vortices. The highest negative velocity on the slat lower surface at $\alpha = 12°$ implies highest vorticity velocity amongst the presented angles of attack. The highest streamwise velocity on the upper side can be seen for $\alpha = 12°$ over the main-element right after the slat gap where the velocity reaches up to twice as much as that of the inlet velocity. The highest velocity on the lower side occurs near the slat cusp where the slat shear layer originates. For all the Baseline cases the maximum value of the crosswise velocity occurs at the slat gap region with increased velocity seen at $\alpha = 12°$. The maximum crosswise velocity lies between the free slat shear layer and the main-element of the 30P30N airfoil for all the presented angles of attack.

The effects of H-SCF on the flow structure within the slat cove region are minimal as the shape and trajectory of the slat shear layer follows the same trend as that of the Baseline case for all the presented angles of attack, however the size of the vortical structures inside the slat cove region has been reduced noticeably. The use of the SCF, leads to the elimination of the large vortices in the slat cove region as their area of development is covered by the SCF. However, closer to the slat trailing-edge on the lower surface of the SCF smaller vortices have emerged. Similar to the Baseline case, the size and magnitude of these vortices are greatly influenced by the angle of attack. These vortices also arise right after the impingement of the slat shear layer into the slat lower surface as previously seen with the Baseline case. Olson [25] showed that the favourable pressure gradient between the slat upper and lower surface at the slat cusp accelerates and energizes the flow, which also influences the strength and trajectory of the slat shear layer. The SCF has completely eliminated this favourable pressure gradient on the lower surface of the slat, thus reducing the energy of the existing limited shear layer. The existing smaller vortices can be completely prevented by having a SCF profile that follows the same profile as that of the slat shear layer trajectory. However, this could prove difficult for practical operation as this slat shear layer trajectory is not only dependant on the angle of attack but also on the operating Reynolds and Mach number. If the SCF profile is larger than the slat shear layer profile then the flow at the slat gap gets restricted, which consequently affects the velocity peak and aerodynamic performances of the main-element. Nevertheless, a SCF profile that eliminates the large vortices in the slat cove region at the same time maintaining the aerodynamic performance is highly favourable as they are viable source of noise reduction, as shown by Imamura *et al* [13, 14], Tao [18] and also in the current experimental study (see Sec. III.C).

Figures. 15 to 18 show the Reynolds stress tensors for the Baseline, H-SCF and SCF cases at the angles of attack $\alpha = 6°$, $8°$, $10°$ and $12°$. The presented results of the normal eddy stress components ($\overline{u'u'}$ and $\overline{v'v'}$) show that the crosswise Reynolds normal stress components ($\overline{v'v'}$) are higher than the streamwise Reynolds normal stress components ($\overline{u'u'}$) for all the presented configurations and angles of attack. The maximum value of the $\overline{u'u'}$ components for all the cases can be found at the originating location of the slat shear layer adjacent to the slat cusp and also at the slat wake. The maximum value of the $\overline{v'v'}$ components can be observed at the slat gap region closer to the suction side of the main-element for both the Baseline and the H-SCF case. However the $\overline{v'v'}$ components for the SCF is slightly reduced at the slat gap region but increased values of it can be observed on the lower surface of the SCF itself. Similar behaviour can be observed at all the presented angles of attack. The results also show that the shear stress distribution for both the normal eddy stress components ($\overline{u'u'}$ and $\overline{v'v'}$) reduces as the angle of attack is increased for all the three configurations.
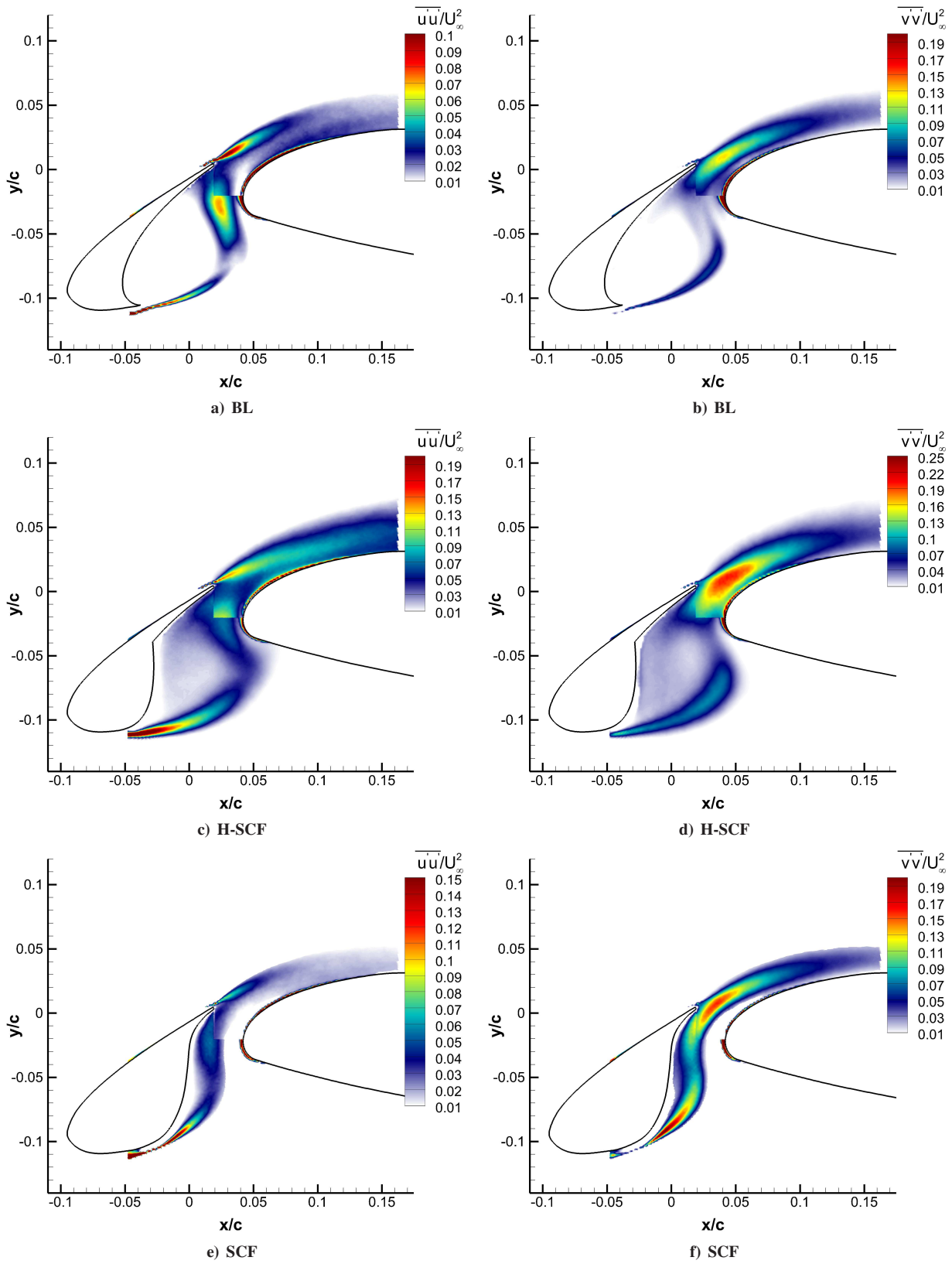
American Institute of Aeronautics and Astronautics

Figure 15. Reynolds stress tensor contours around slat the region for $\alpha = 6°$ **with a flow velocity of** $U_\infty = 30$ **m/s,** $Re_c = 7.0 \times 10^5$.

Figure 16. Reynolds stress tensor contours around slat the region for $\alpha = 8°$ **with a flow velocity of** $U_\infty = 30$ **m/s,** $Re_c = 7.0 \times 10^5$.

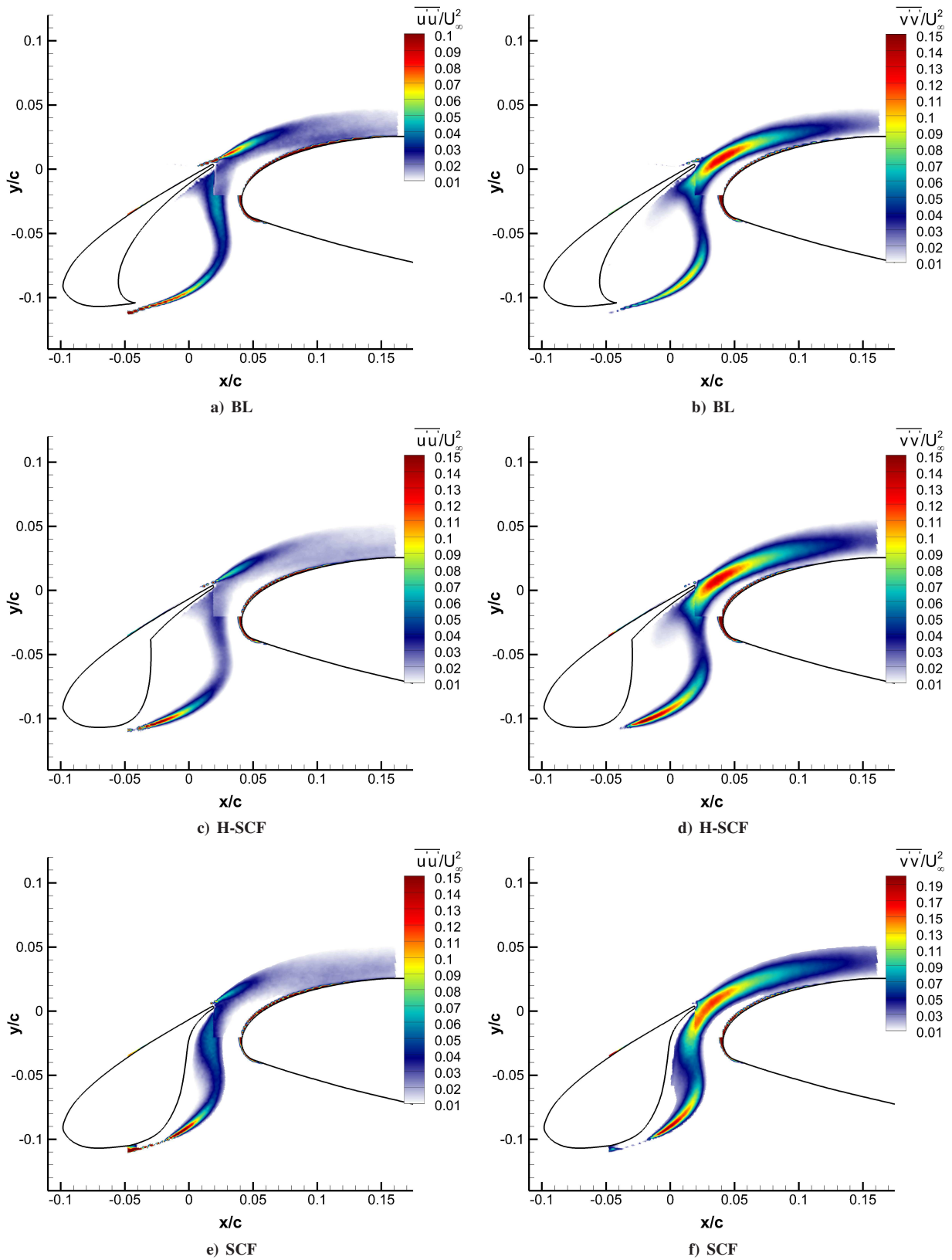American Institute of Aeronautics and Astronautics

Figure 17. Reynolds stress tensor contours around slat the region for $\alpha = 10°$ **with a flow velocity of** $U_\infty = 30$ **m/s,** $Re_c = 7.0 \times 10^5$.
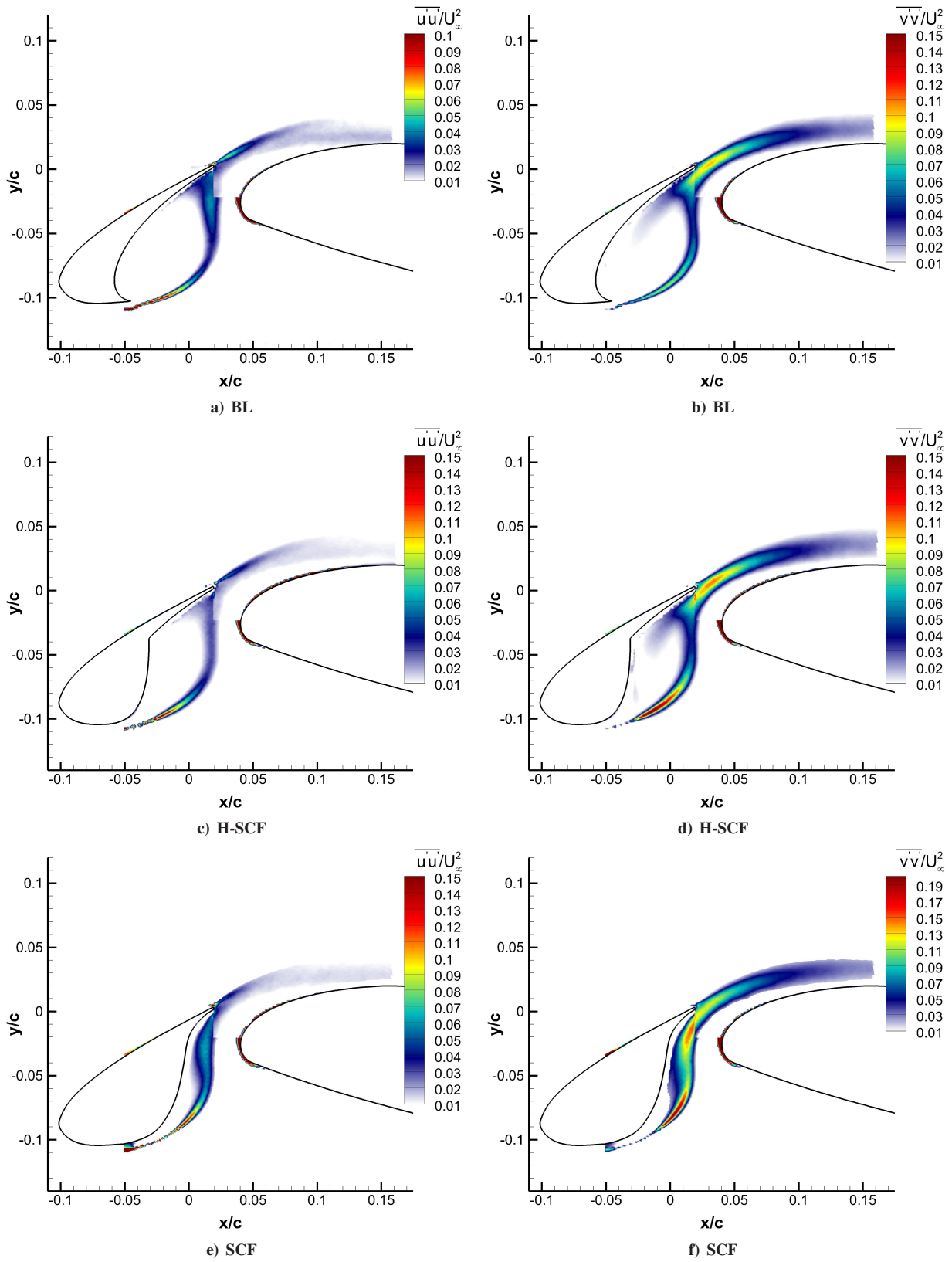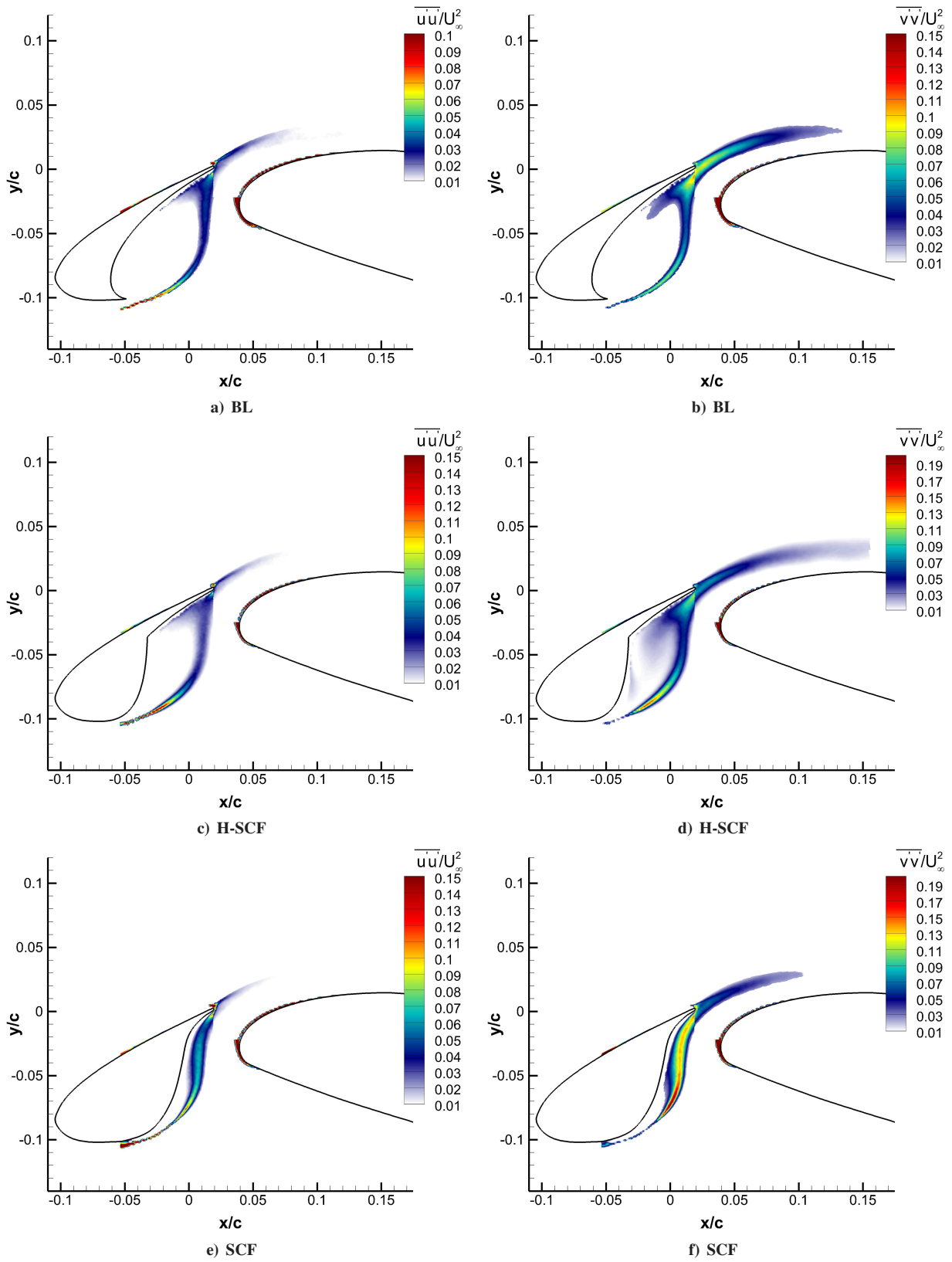
American Institute of Aeronautics and Astronautics

Figure 18. Reynolds stress tensor contours around slat the region for $\alpha = 12°$ **with a flow velocity of** $U_\infty = 30$ **m/s,** $Re_c = 7.0 \times 10^5$**.**

C. Aeroacoustic Charactersitics

a) $\alpha = 6°$

b) $\alpha = 8°$
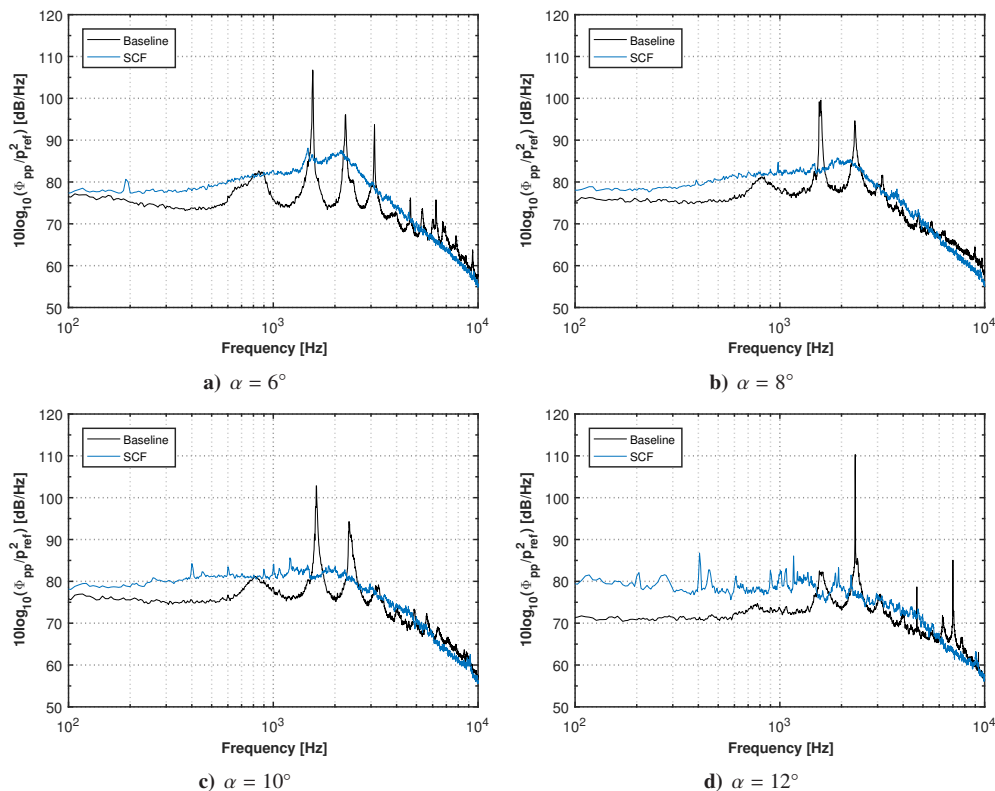
c) $\alpha = 10°$

d) $\alpha = 12°$

Figure 19. Pressure fluctuations spectra for the surface transducer M1 (x = 22.414 mm) at main-element leading-edge of a 30P30N airfoil with slat modifications, for a flow velocity of U_∞ = 47 m/s, Re_c = 1.1 × 10⁶.

The unsteady surface pressure measurements were acquired on the main-element and flap surface using 21 flush-mounted pressure transducers placed at various locations that are detailed in Fig. 4 and Table. 2. The data were acquired for 32 s and sampled at 40 kHz. The presented wall-pressure spectra results were obtained by discrete power spectral density (PSD) of the pressure signals using Hanning window and was averaged 200 times to yield a frequency resolution of Δf = 6.25 Hz. For the purpose of brevity, only selected results from transducers M1 and M6 on the main-element and F1 on the flap are presented and discussed here. From the aeroacoustic study carried out by Murayama *et al*, it can be seen that the sensors on the main-element are sufficient enough to clearly capture the narrowband and broadband spectra of the vortical fluctuations within the slat cove. The results from the unsteady surface pressure measurements from the transducer M1 at the leading edge of the main-element are shown in Fig. 19. The results are not available for the Droop-slat configuration for this particular location since the transducers were covered by the Droop-slat profile. The Baseline results show distinct narrowband peaks for all the presented angles of attack with varying intensities. Three distinct peaks in the mid-range frequency are observed for $\alpha = 6°$ with spectral levels up to 107 dB, 96 dB and 93 dB at frequencies f = 1.6 kHz, 2.3 kHz and 3.1 kHz, respectively. At $\alpha = 8°$ and 10° only two distinct narrowband peaks with spectral levels of about 103 dB and 94 dB at f = 1.6 kHz and 2.3 kHz are observed. The spectral intensity further increases to 110 dB and occurrence reduces to a single narrowband peak at f = 2.3 kHz for $\alpha = 12°$. Even though the emergence of the narrowband components in the mid-range frequency has reduced from three to one at $\alpha = 12°$, a noticeable narrowband peak with lower spectral intensity of 86 dB at f = 7 kHz has emerged. The results also show that the application of the SCF completely eliminates all the narrowband spectra observed for all the Baseline cases, but a near-field narrowband bump between mid-range frequencies f = 1 kHz and 3 kHz has appeared. Therefore, the narrowband peaks can now be directly related to the vortical structures within the slat cove region previously discussed in the flow visualisation results, and also, the elimination of the narrowband peaks also corresponds to the elimination of the large vortical structures by the SCF. The intensity of the observed spectral levels can also be directly related to the size and energy of the vortical structures. Eventhough the narrowband peaks were eliminated by the application of SCF, an increase in the broadband spectrum of up to 10 dB can be observed at low-mid frequency range. The increased broadband spectrum below 2 kHz especially at $\alpha = 12°$ can be attributed to the
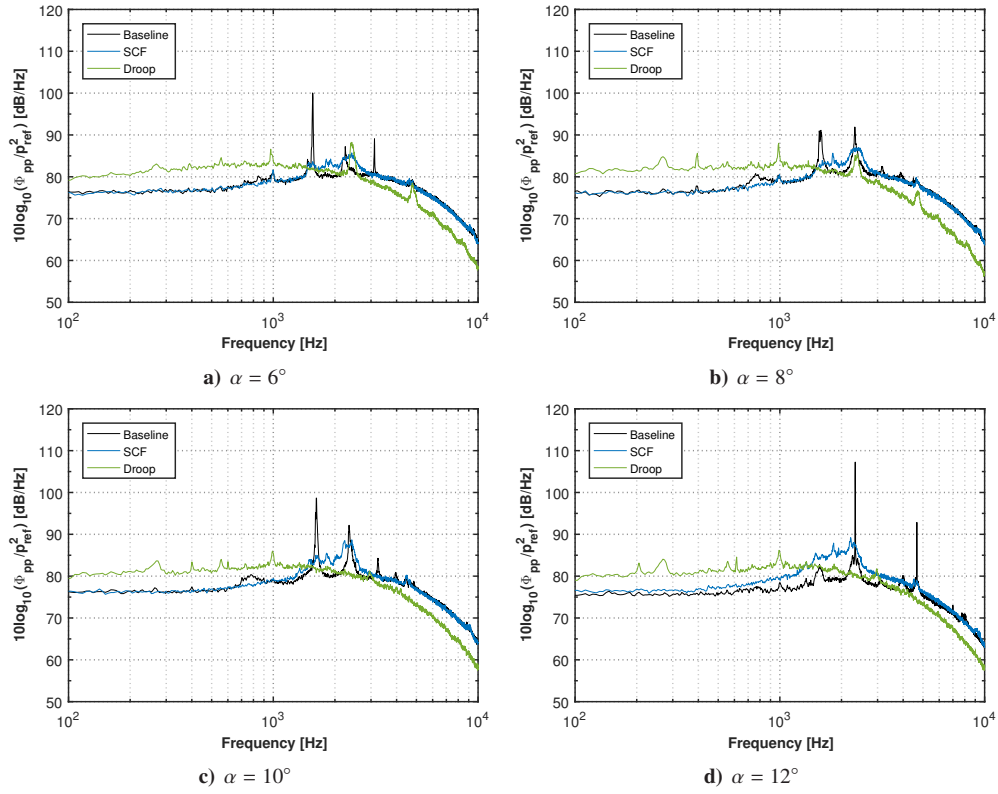
Figure 20. Pressure fluctuations spectra for the surface transducer M6 (x = 239.701 mm) at main-element trailing-edge of a 30P30N airfoil with slat modifications, for a flow velocity of U_∞ = 47 m/s, Re_c = 1.1 × 10⁶.

increased impingement of the flow on to the slat trailing-edge due to the slat cove flow path.

The unsteady surface pressure fluctuations from the transducers M6 at the trailing-edge of the main-element and F1 at the flap leading-edge are shown in Figs. 20 and 21, respectively. Unlike the multiple narrowband peaks observed at the transducer M1, only two dominant narrowband peaks were observed at all the presented angles of attack for the Baseline case. These two narrowband peaks at frequencies f = 1.6 kHz and 2.3 kHz were also observed at the flap leading-edge transducer F6. The results here do not show an overall increase in the broadband spectra for the SCF case compared to the Baseline case as seen at the transducer M1 on the leading-edge of the main-element. Further far-field measurements are needed to verify weather the narrowband bump and broadband noise are increased at the far-field location for the SCF case or if they are only local near-field effects. For the Droop-slat configuration, the narrowband peaks are completely absent with an increase in the broadband spectra of up to 5 dB for frequencies below f = 1.1 kHz for all the presented angles of attack. The streamwise coherence between the two transducers were calculated using Eq. 1, where N is the number of transducers and the data was averaged 2000 times yielding a frequency resolution of Δf = 62.5 Hz. The streamwise coherence for the Baseline case between the transducers M1-M6, M1-F1, and M1-F6 at spanwise location z = 277 mm are presented in Fig. 22. The coherence between the selected transducers shows that the narrowband peaks observed in the wall-pressure spectra of M6, F1 and F6 were convected from the slat cove region having strong vortical fluctuations, which was initially observed at M1. The narrowband bumps for the SCF in Fig. 23 shows a weak coherence of the turbulence structures between the upstream transducers M1-F1 and M1-F6 between f = 1.6 kHz and 2.3 kHz that are convected from the slat.

$$\gamma^2_{p_i p_j}(f) = \frac{|\,G_{p_i p_j}(f)\,|^2}{|\,G_{p_i p_i}(f)\,\|\,G_{p_j p_j}(f)\,|} \quad \text{for } p_i = 1 \text{ and } p_j = 1, 2, 3, ..., N. \tag{1}$$

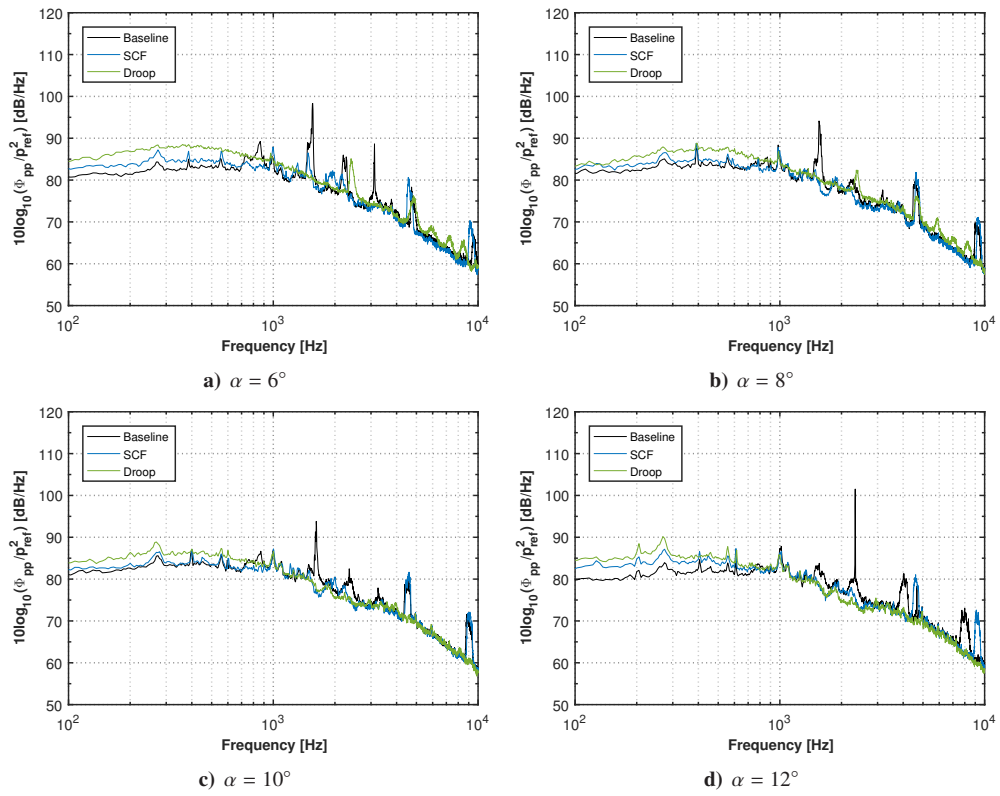American Institute of Aeronautics and Astronautics

Figure 21. Pressure fluctuation spectra for the surface transducer F1 ($x = 308.844$ mm) at flap leading-edge of a 30P30N airfoil with slat modifications, for a flow velocity of $U_\infty = 47$ m/s, $Re_c = 1.1 \times 10^6$.

Figure 22. Coherence between the reference transducer M1 and transducers M6 on the main-element, F1 on the flap leading-edge and F6 on the flap mid-chord at location $z = 277$ mm for the Baseline.

American Institute of Aeronautics and Astronautics

a) $\alpha = 6°$

b) $\alpha = 8°$

c) $\alpha = 10°$
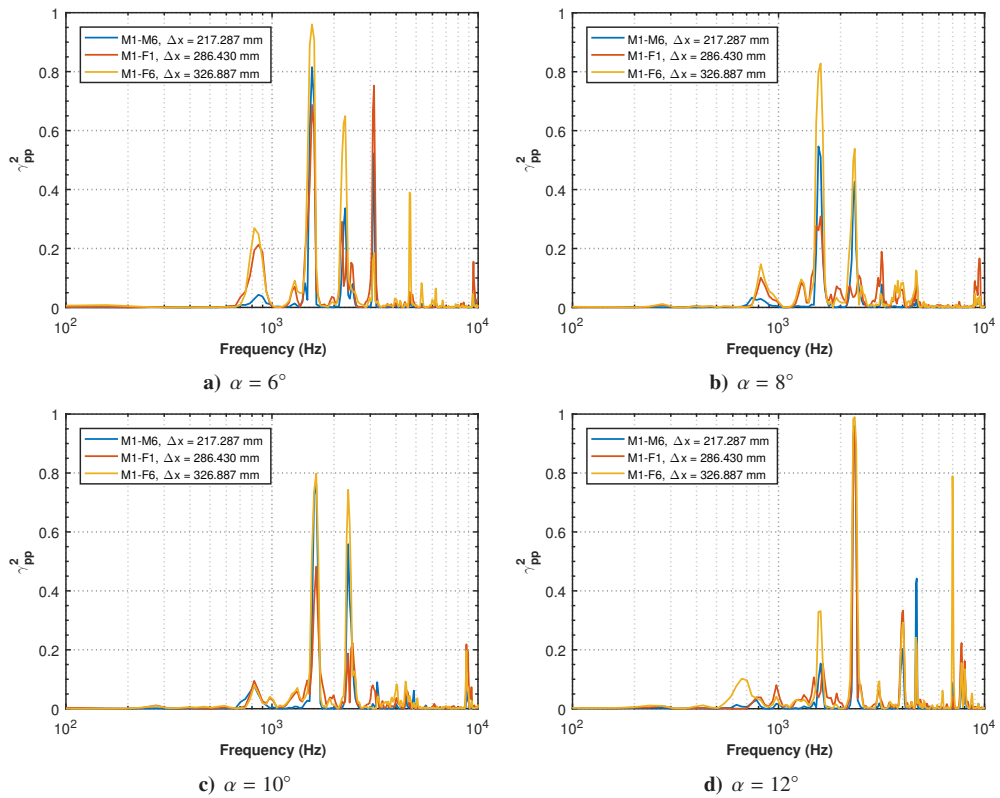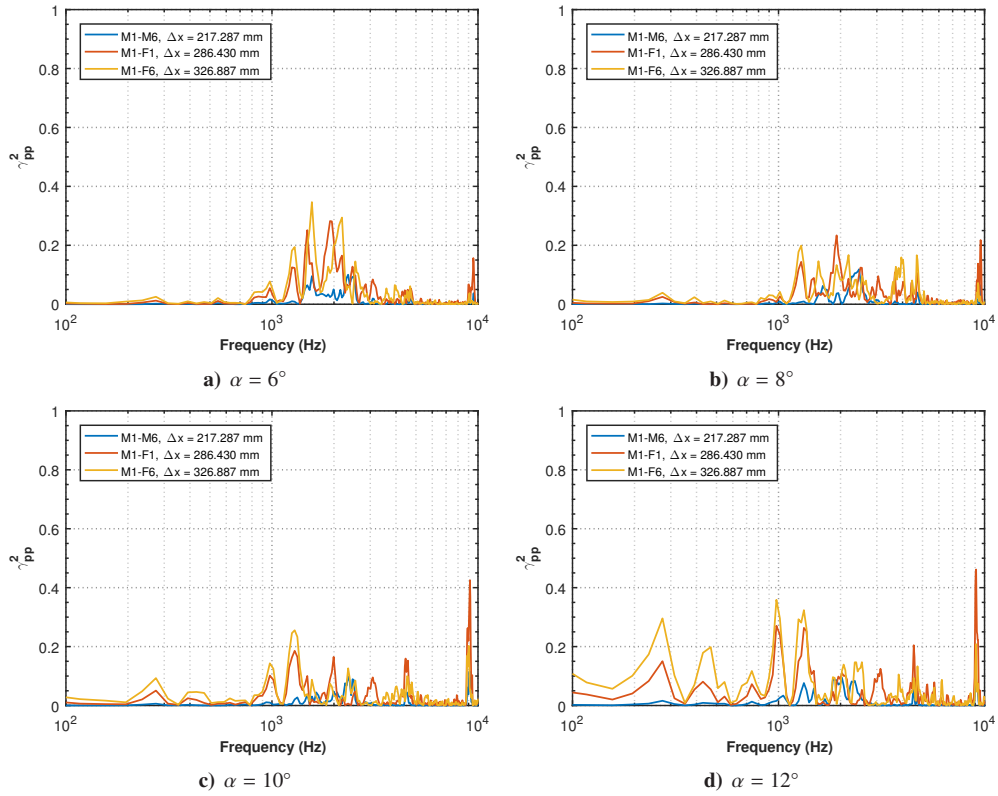

d) $\alpha = 12°$

Figure 23. Coherence between the reference transducer M1 and transducers M6 on the main-element, F1 on the flap leading-edge and F6 on the flap mid-chord at location $z = 277$ mm for the SCF.

IV.   Conclusion

A three-element 30P30N airfoil with a retracted chord of $c = 0.35$ m and span of $l = 0.53$ m has been experimentally tested and reported for three different configurations, namely Baseline, H-SCF, SCF and Droop-slat. Detailed aerodynamic and aeroacoustic results for angles of attack $\alpha = 6°$, $8°$, $10°$ and $12°$ at $Re_c = 7 \times 10^5$ were presented. The C_p distribution shows a very similar characteristics between the Baseline and SCF cases. However, the suction peak on the main-element for the SCF cases are very sensitive to the angle of attack based on the SCF profile used. As expected the Droop-slat configuration has a completely different aerodynamic characteristics compared to the other two cases. The suction peak for the Droop-slat case is reduced by up to 50% relative to the Baseline. The flow visualisation results of the Baseline case showed a large fixed vortices present within the slat-cove region for all the presented angles of attack. This large vortices was eliminated by the application of SCF, however, smaller vortices developed on the lower surface of the SCF. The H-SCF reduces the size of the slat cove vortices noticeably but the slat shear layer trajectory was very similar to the Baseline case. The wall-pressure spectra on leading-edge of the main-element for the Baseline case shows multiple narrowband peak components, which corresponds to the slat fixed vortices. These narrowband peaks have been completely eliminated by the application of SCF but it increases the overall broadband spectra up to 10 dB at lower frequencies < 1 kHz. The results from the application of morphing slat cove structures have showed improvement in aeroacoustic characteristics of the tested high-lift airfoil.

American Institute of Aeronautics and Astronautics

References

[1] Ai, Q., Azarpeyvand, M., Lachenal, X., and Weaver, P. M., "Aerodynamic and Aeroacoustic Performance of Airfoils with Morphing Structures," *Wind Energy*, Vol. 19, No. 7, 2016, pp. 1325–1339.

[2] Ai, Q., Kamliya Jawahar, H., and Azarpeyvand, M., "Experimental Investigation of Aerodynamic Performance of Airfoils Fitted with Morphing Trailing Edges," *AIAA Paper 2016-1563*, 2016.

[3] Showkat Ali, S. A., Liu, X., and Azarpeyvand, M., "Bluff Body Flow and Noise Control Using Porous Media," *AIAA Paper 2016-2754*, 2016.

[4] Showkat Ali, S. A., Szoke, M., Azarpeyvand, M., and Ilário, C., "Trailing Edge Bluntness Flow and Noise Control Using Porous Treatments," *AIAA Paper 2016-2832*, 2016.

[5] Afshari, A., Azarpeyvand, M., Dehghan, A. A., and Szoke, M., "Trailing Edge Noise Reduction Using Novel Surface Treatments," *AIAA 2016-2834*, 2016.

[6] Liu, X., Kamliya Jawahar, H., Azarpeyvand, M., and Theunissen, R., "Aerodynamic and Aeroacoustic Performance of Serrated Airfoils," *AIAA Paper 2015-2201*, 2015.

[7] Liu, X., Kamliya Jawahar, H., Azarpeyvand, M., and Theunissen, R., "Wake Development of Airfoils with Serrated Trailing Edges," *AIAA Paper 2016-2817*, 2016.

[8] Lyu, B., Azarpeyvand, M., and Sinayoko, S., "Prediction of Noise from Serrated Trailing-Edges," *Journal of Fluid Mechanics*, Vol. 793, 2016, pp. 556–588.

[9] Horne, W. C., James, K. D., Arledge, T. K., Soderman, P. T., Field, M., Burnside, N., and Jaeger, S. M., "Measurement of 26%-scale 777 airframe noise in the NASA Ames 40- by 80 foot wind tunnel," *AIAA 2005-2810*, California, 2005.

[10] Streett, C., Casper, J., Lockard, D., Khorrami, M., Stoker, R., Elkoby, R., Wenneman, W., and Underbrink, J., "Aerodynamic Noise Reduction for High-Lift Devices on a Swept Wing Model," *AIAA 2006-212*, 2006.

[11] Andreou, C., Graham, W., Shin, H.-c., Street, T., Member, S., and Lecturer, S., "Aeroacoustic study of airfoil leading edge high-lift devices," *AIAA 2006-2515*, 2006.

[12] Andreou, C., Graham, W., Shin, H.-c., Introduction, I., Street, T., Member, S., and Lecturer, S., "Aeroacoustic Comparison of Airfoil Leading Edge High-Lift Geometries and Supports," *AIAA 2007-230*, 2007.

[13] Imamura, T., Ura, H., Yokokawa, Y., Enomoto, S., Yamamoto, K., Hirai, T., Group, A. P., and Division, E. S., "Designing of Slat Cove Filler as a Noise Reduction Device for Leading-edge Slat," *AIAA 2007-3473*, 2007.

[14] Ura, H., Yokokawa, Y., Imamura, T., Ito, T., and Yamamoto, K., "Investigation of Airframe Noise from High Lift Configuration Model," *AIAA 2008-19*, 2008.

[15] Shmilovich, A., Yadlin, Y., and Pitera, D. M., "Wing Leading Edge Concepts for Noise Reduction," *27th International Congress of the Aeronautical Sciences (ICAS)*, 2010.

[16] Shmilovich, A., Yadlin, Y., and Company, T. B., "High-lift systems for enhanced take-off performance," *28th International Congress of the Aeronautical Sciences*, 2012, pp. 1–13.

[17] Scholten, W. D., Hartl, D. J., Turner, T. L., and Kidd, R. T., "Development and Analysis-Driven Optimization of Superelastic Slat-Cove Fillers for Airframe Noise Reduction," *AIAA Journal*, dec 2015, pp. 1–17.

[18] Tao, J. and Sun, G., "A novel optimization method for maintaining aerodynamic performances in noise reduction design," *Aerospace Science and Technology*, Vol. 43, 2015, pp. 415–422.

[19] Garcia-Sagrado, A. and Hynes, T., "Wall-Pressure Sources Near an Airfoil Trailing Edge Under Separated Laminar Boundary Layers," *AIAA Journal*, Vol. 49, No. 9, 2011, pp. 1841–1856.

[20] Garcia-Sagrado, A. and Hynes, T., "Stochastic estimation of flow near the trailing edge of a NACA0012 airfoil," *Experiments in Fluids*, Vol. 51, No. 4, 2011, pp. 1057–1071.

[21] Garcia-Sagrado, A. and Hynes, T., "Wall pressure sources near an airfoil trailing edge under turbulent boundary layers," *Journal of Fluids and Structures*, Vol. 30, 2012, pp. 3–34.

[22] Valarezo, W. O., "High-lift testing at high Reynolds numbers," *AIAA-92-3986*, 1992.

[23] Valarezo, W. O., Dominik, C. J., and Mcghee, R. J., "Reynolds and Mach number effects on multielement airfoils," *N93-27446*, 1992.

[24] Chin, V. D., Peters, D. W., Sdaid, F. W., and Mcghee, R. J., "Flowfield Measurements About a Multi-Element Airfoil At High Reynolds Numbers," *AIAA-93-3137*, 1993.

[25] Olson, S., Thomas, F., and Nelson, R., "A preliminary investigation into slat noise production mechanisms in a high-lift configuration," *AIAA 2000-4508*, 2000.